Inverse Design of Self-Assembling Diamond Photonic Lattices from Anisotropic Colloidal Clusters

Yutao Ma, Joseph C. Aulicino, and Andrew L. Ferguson*

Pritzker School of Molecular Engineering, University of Chicago, Chicago, IL, 60637

E-mail: andrewferguson@uchicago.edu

Phone: (773) 702-5950

Abstract

Colloidal nanoparticles with anisotropic interactions are promising building blocks for the fabrication of complex functional materials. A challenge in the self-assembly of colloidal particles is the rational design of geometry and chemistry to program the formation of a desired target structure. We report an inverse design procedure integrating Langevin dynamics simulations and evolutionary algorithms to engineer anisotropic patchy colloidal clusters to spontaneously assemble into a cubic diamond lattice possessing a complete photonic band gap. The combination of a tetrahedral cluster geometry and optimized placement of a single type of anisotropic interaction patch results in a colloidal building block predicted to assemble a cubic diamond lattice with more than 82% yield. This design represents an experimentally viable colloidal building block capable of high fidelity assembly of a cubic diamond lattice.

1 Introduction

Colloidal particles are promising building blocks that can self-assemble into complex functional materials. ^{1–10} Self-assembled colloidal crystals ^{4–7,10–13} have drawn great research interest, with a particular focus on open crystal lattices such as pyrochlore, diamond, and inverse opal that possess complete photonic band gaps ^{14–18} and are of interest as 3D photonic crystals with applications as optical wave guides and in optical computing. ^{14,17–21} In experimental studies, triblock patchy colloids equipped with hydrophobic and electrostatic interactions have been used to form two-dimensional Kagome lattices ⁴ and colloids decorated with DNA strands have been utilized to form MgCu₂ and diamond lattices. ^{10,22} Very recently, compressed tetrahedral colloidal clusters employing a combination of adhesive interactions and steric interlocking have been used to realize a high-density cubic diamond lattice with a complete photonic bandgap. ²³ In computer simulations, colloids with various forms of interactions have been simulated and predicted to give rise to pyrochlore lattice, ⁵ diamond lattice, ^{6,7,13,24} hexagonal tetrastack lattice ¹¹ and binary nanoparticle crystals. ²⁵

A key aspect of the study of self-assembling colloidal lattices is the design of experimentally-realizable building blocks programmed to assemble desired target structures. Many inverse design techniques have been proposed for colloidal particles. 9,26-34 For example, Lindquist et al. 28 have used a machine-learning approach based on relative entropy coarse graining to design the isotropic interactions between colloids that can favor the formation of various lattices. Marcotte et al. 33 have used statistical-mechanical method to design isotropic interactions whose ground states are the target structures. Romano and Sciortino 26 have proposed incorporating patterning asymmetry into patchy colloid design to favor pyrochlore lattice. Morphew et al. 7 have used a basin-hopping optimization algorithm to find optimal triblock patchy colloids that favor the formation of cubic diamond and body centered cubic lattices composed of colloidal clusters. A primary challenge in the inverse design problem is the coexistence of crystal structures with similar thermodynamic stabilities. This typically results in the formation of polymorphic or hybrid crystal structures instead of the pure

target lattice. For example, the pyrochlore lattice has a closely-related analogue known as the hexagonal tetrastack lattice which differs in the orientation of adjacent layers but has similar free energy ²⁶ and the cubic diamond lattice has a nearly equally stable analogue in the hexagonal diamond lattice. ⁶ Simulations by Rao et al. ³⁵ demonstrated that triblock patchy colloids form a stacking hybrid of pyrochlore and hexagonal tetrastack lattices during two-stage temperature cooling. Similarly, Romano et al. ⁶ show that Kern-Frenkel patchy colloids may form a mixture of cubic diamond and hexagonal diamond lattices.

We have previously developed an inverse design protocol termed landscape engineering that sculpts the free energy surface governing the self-assembly of patchy colloids and used this approach to find optimal design parameters that favor the formation of pyrochlore and cubic diamond lattices. This design strategy relied on relatively intricate placement of patches on the surface of spherical patchy colloids requiring multiple specific patch types and a two-stage hierarchical assembly mechanism. Using this approach, we discovered patchy colloid designs capable of assembling defect-free pyrochlore and cubic diamond lattices, but the relatively complex design of the particles placed them at the very edge of what is experimentally achievable even with state-of-the-art fabrication techniques.

In this paper, we follow up on this work employing a simpler inverse-design protocol and a simplified design space more amenable to experimental realization. We target an open cubic diamond lattice and restrict our designs to a single patch type placed upon pre-assembled clusters of spherical patchy colloids within a rigid tetrahedral tetramer. Many surface-patterning techniques have been developed recently to decorate the surfaces of colloids with functional materials ^{37–39} and recent experimental advances have realized the fabrication of colloidal clusters. ^{40–43} The geometry of the tetrahedral colloidal cluster compensates for the loss of design flexibility associated with restricting ourselves to a single patch type. Using this strategy we report a design for an experimentally-realizable anisotropic patchy colloidal cluster that exhibits in excess of 82% yield of the open cubic diamond lattice.

The remainder of this paper is structured as follows. In the next section we describe

our computational model for the colloidal particles, Langevin dynamics simulations, and our inverse design strategy based on evolutionary algorithm. In the following section we describe the results of our inverse design approach and the validation that tetrahedral tetramers composed of patchy colloids with optimal patch design can self-assemble into the target cubic diamond lattice with high fidelity. Finally, we present our conclusions and outlook for future work.

2 Methods

2.1 Cubic diamond lattice

He et al. recently demonstrated the experimental realization of a cubic diamond lattice composed of compressed tetrahedral tetramers in which the triangular faces of neighboring tetramers are induced to adopt the requisite crystal structure through a combination of complementary DNA attractions and steric excluded volume interactions. ²³ The close packing between the faces of adjacent tetramers results in a particle volume fraction of 68% and, for sufficiently high refractive index contrasts, is expected to possess a complete photonic bandgap. It is the goal of the present work to engineer tetrahedral colloids to instead assemble a closely related cubic diamond lattice in which neighboring tetramers interact via their vertices rather than their faces to produce an open crystal with a 12% particle volume fraction. This crystal lattice – in which the geometric centers of tetrahedral tetramers sit on the lattice sites of an ordinary cubic diamond lattice, and hereafter simply referred as cubic diamond lattice for brevity – possesses a complete photonic band gap at relatively low relative permittivity and low band indices. 7,17-20,36 Lattice constants on micron length scales place the band gap within the visible or near-infrared regime of the electromagnetic spectrum. 17,36,44 This has made this open cubic diamond lattice formed from colloids of particular technological interest in optical applications such as optical wave guiding and optical computing, 17,19,20 but its robust fabrication by bottom-up assembly remains an enduring challenge. 6,7,36

The basic motif of cubic diamond lattice is the chair-like ring (Figure 1a) composed of six staggered dimers.⁷ Each staggered dimer (Figure 1b) comprises two tetrahedral tetramers whose bases are rotated by 60° with respect to each other.

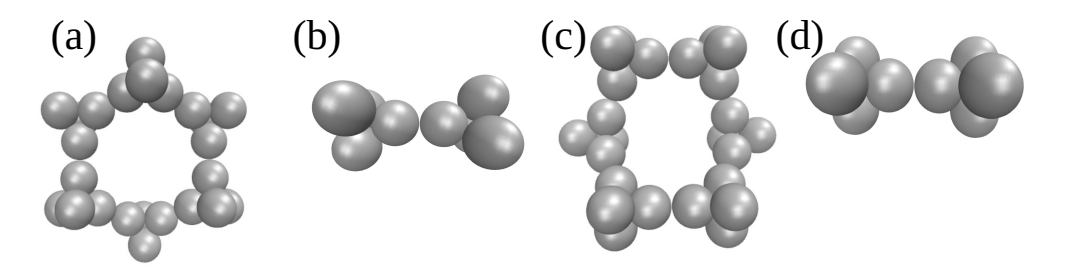


Figure 1: Structure of cubic and hexagonal diamond lattices. (a) Chair-like ring. The chair-like ring is the fundamental motif of the cubic diamond lattice. (b) Staggered dimer of tetrahedral tetramers. Each contiguous pair of tetrahedral tetramers in the cubic diamond lattice exists as a staggered dimer in which the base of one tetramer is azimuthally rotated through 60° relative to the other along the axis joining their centers of mass. (c) Boat-like ring. The hexagonal diamond lattice comprises 25% chair-like rings and 75% boat-like rings. (d) Eclipsed dimer of tetrahedral tetramers. Of the six tetrahedral tetramer dimers in the boat-like ring, two are eclipsed and four are staggered.

A polymorphic analogue of cubic diamond lattice is the hexagonal diamond lattice in which 25% of the rings are chair-like (Figure 1a) and 75% of the rings are boat-like (Figure 1c). In a boat-like ring, two out of six dimers are eclipsed (Figure 1d) wherein the bases of two constituent tetrahedral tetramers are aligned with each other. Compared to the cubic diamond lattice, the hexagonal diamond lattice possesses smaller photonic band gap occurring at higher band indices, ⁴⁴ making it less desirable for optical applications than cubic diamond lattice. The hexagonal diamond lattice possesses a very similar free energy to the cubic diamond lattice, making it hard to thermodynamically favor the cubic diamond lattice over the hexagonal diamond lattice. Similar concerns apply to the pyrochlore lattice versus hexagonal tetrastack lattice (a hexagonal polymorphic analogue of pyrochlore lattice), in which the hexagonal tetrastack lattice possesses smaller photonic band gap at higher band indices but has similar free energy as the pyrochlore lattice. ³⁵ The similar stabilities of competing polymorphs of open lattices has been a principal challenge in the bottom-up

assembly of defect-free crystals with desirable band structures.

2.2 Anisotropic patchy colloid building blocks

Advanced experimental techniques have enabled fabrication of colloidal clusters with high yield and fidelity 10,40-43 and the surfaces of the constituent colloids forming these colloidal clusters can also be anisotropically functionalized to program the hierarchical assembly into more complex structures. 10,45 In our prior work, 36 we used an inverse design strategy known as landscape engineering to discover a design for spherical patchy colloids to assemble a cubic diamond lattice by a two-stage hierarchical process: (i) the high-temperature assembly of groups of four patchy colloids into tetrahedral tetramers followed by (ii) the low-temperature assembly of these tetrahedral tetramers into a cubic diamond lattice. The two-stage hierarchical assembly mechanism and required rigidity of the tetrahedral tetramers necessitated a relatively complex colloid design possessing nine patches of three different types with different interaction potentials and patch-patch specificities. In the present work, we greatly simplify the design problem in two ways. First, we adopt as the fundamental building block a patchy tetrahedral tetramer as opposed to a spherical colloid and optimize the single-step assembly of tetrahedral tetramers into the cubic diamond lattice. Second, we functionalize the colloids using only a single patch type. We previously used three patch types and employed complementarity between patch types to stabilize the staggered (Figure 1a) over the eclipsed (Figure 1c) dimer configurations to favor the cubic diamond lattice over the hexagonal. In the present work, we show that by adjusting the protrusion of the interaction patches above the surface of the colloid we may exploit excluded volume interactions to preferentially stabilize the staggered dimer configuration using only a single patch type. These two simplifications are motivated by experimental advances in the fabrication of rigid colloidal clusters ("colloidal molecules") with quite complex geometries, including the tetrahedral tetramer, 40-43,46,47 and sophisticated surface-patterning techniques to precisely functionalize the surfaces of colloids with anisotropic interaction patches composed of organic, inorganic, or biological materials.^{37–39,48} Conceptually, we reduce the complexity in the anisotropic interaction patches (i.e., going from three patch types to one) at the expense of increased complexity in the colloid shape (i.e., tetrahedral colloidal building blocks rather than spherical ones) to design a building block that is more readily accessible to existing experimental techniques.

We model the patchy colloidal particles using a similar approach to that detailed in Ref. ³⁶ Each tetramer is treated as a tetrahedral assembly of four spherical colloids (type "A" particles) that move as a rigid body. Figure 2a illustrates a tetrahedral tetramer dimer in a staggered configuration wherein the base of one tetrahedral tetramer is azimuthally rotated through 60° with respect to the other along the axis connecting their centers of mass. The surface of each spherical colloid is functionalized with three anisotropic interaction patches (type "B" particles) in an equilateral triangle arrangement as illustrated in Figure 2b. The "B" patches are located at a polar angle ϕ_B from the pole of each "A" colloid. The placement of each patch on each colloid in the tetrahedral cluster is identical such that the tetrahedral tetramer is tetrahedrally symmetric. The "B" interaction patches are represented as Lennard-Jones spheres on the surface of the "A" colloid. The degree of protrusion of the "B" patches is quantified by the protrusion ratio $\alpha_B = d_{AB}/R_A$, where d_{AB} is the distance between the center of the "B" patch and the center of the "A" colloid and R_A is the radius of the "A" colloid. A protrusion ratio of $\alpha_B = 1$ indicates that the center of the "B" sphere is coincident with the surface of the "A" colloid, a value of $\alpha_B = (1 + R_B/R_A)$ indicates that the "B" sphere lies tangent upon (i.e., "kisses") the "A" colloid, and a value of $\alpha_B=(1-R_B/R_A)$ indicates that the "B" patch is buried just below the surface of the "A" colloid. Controlling the protrusion ratio of the patch enables us to stabilize the staggered dimer of tetrahedral tetramers using a single patch type by favoring interlocking configurations of the patches at the interface as shown in Figure 2c. Figure 2d presents a schematic drawing of the colloidal particle architecture illustrating ϕ_B and α_B .

We model the patch-patch ("B"-"B") interactions between the spherical patches with a

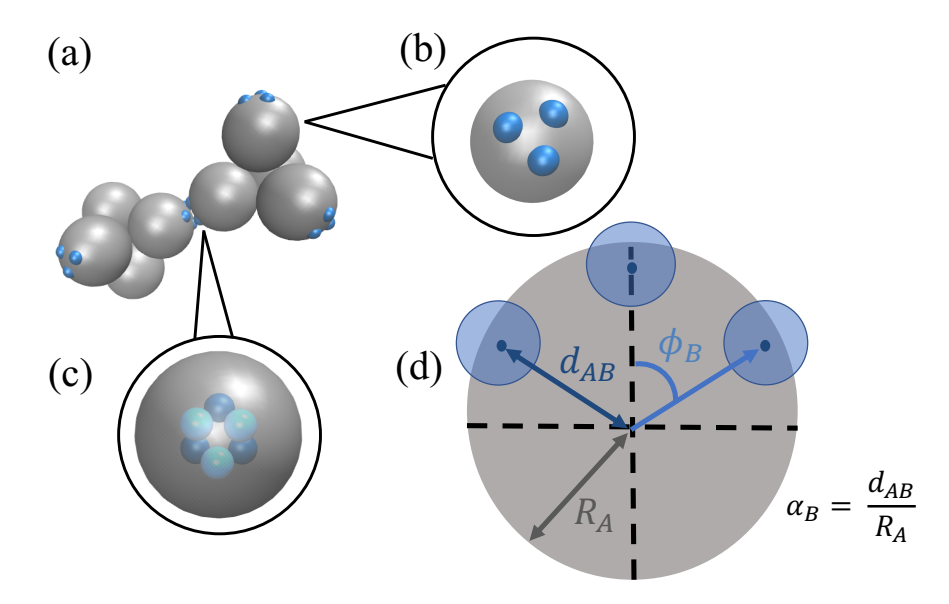


Figure 2: Computational model of the patchy colloid tetrahedral tetramers. (a) A staggered dimer of tetrahedral tetramers showing the colloids ("A" particles, grey) functionalized with anisotropic surface patches ("B" particles, blue). (b) A zoomed-in view of a single spherical patchy colloid belonging to one of the tetrahedral tetramers. The interaction patches are modeled as Lennard-Jones spheres placed in an equilateral triangle configuration at a tunable surface depth. (c) A zoomed-in view of the staggered dimer interface between the two tetrahedral tetramers along the axis connecting their centers of mass. The dark blue spheres represent the surface patches in one of the tetrahedral tetramers and the light blue spheres to those in the other. An interlocked configuration of the surface patches favors the staggered dimer configuration. (d) A schematic diagram of a patchy colloid illustrating the polar angle ϕ_B and protrusion ratio α_B of the surface patches. The transparent blue circles represent the patches and the dark blue dots represent the centers of patches. d_{AB} is the distance between the center of colloid and the center of patch and R_A is the radius of colloid. The protrusion ratio α_B is defined as $\alpha_B = d_{AB}/R_A$. All molecular renderings in this figure and throughout the paper are constructed using Visual Molecular Dynamics (VMD). ⁴⁹

Lennard-Jones potential,

$$U_{\rm LJ}^{BB}(r) = 4\varepsilon_B \left[\left(\frac{\sigma_B}{r} \right)^{12} - \left(\frac{\sigma_B}{r} \right)^6 \right],\tag{1}$$

where r is the center of mass distance between the "B" spheres, ε_B is the well depth controlling the interaction strength, and σ_B is the patch diameter. Following our previous work we choose the colloid to be five times larger than the surface patches such that $\sigma_A = 5\sigma$ and $\sigma_B = \sigma$. The colloid-colloid ("A"-"A") and colloid-patch ("A"-"B") interactions are treated by a surface-shifted Weeks-Chandler-Andersen (WCA) potential 50 to model excluded-volume interactions,

$$U_{\text{WCA}}^{ij}(r) = \begin{cases} 4\varepsilon_{ij} \left[\left(\frac{\sigma}{r - \Delta_{ij}} \right)^{12} - \left(\frac{\sigma}{r - \Delta_{ij}} \right)^{6} \right] + \varepsilon_{ij} & \text{if } r < 2^{\frac{1}{6}}\sigma + \Delta_{ij}, \\ 0 & \text{if } r \geq 2^{\frac{1}{6}}\sigma + \Delta_{ij}, \end{cases}$$
(2)

where ε_A is the well depth controlling the interaction strength for the "A"-"A" interaction, $\varepsilon_{ij} = \sqrt{\varepsilon_i \varepsilon_j}$ is given by the Lorentz-Berthelot mixing rule, and $\Delta_{ij} = (\sigma_i + \sigma_j)/2 - \sigma$ shifts the potential to act between the surfaces of particles i and j. The assembly of four "A" colloids and 12 "B" patches comprising the tetrahedral tetramer is treated as a rigid body and interactions between particles in the same rigid body are neglected.

Our patchy colloid model is inspired by the anisotropic patterning symmetry model introduced by Romano and Sciortino²⁶ and shares similarities with this model in that it introduces anisotropy into the colloid-colloid interaction interface to preferentially stabilize the staggered dimer conformation. This prior work treated the anisotropic interactions through a triangular patch flush to the surface of the colloid and modeled by an extension of the Kern-Frenkel potential that places anisotropic interaction sites at the three vertices of the patch. ^{26,51} A staggered interface was preferentially stabilized by maximizing the overlap of two contacting patches in order to achieve the most favorable interaction energy. Our model also employs a triangular patch geometry but differs from the patterning symmetry model

in that the patch comprises three spherical and isotropic interaction sites that are raised above the surface of the colloidal sphere. The desired staggered dimer interface exploits the topography of the patch to stabilize the desired staggered dimer conformation through a combination of both steric interlocking and favorable interaction energies (Figure 2c) and in this respect shares similarities with the mechanism exploited in the recent experimental work of He et al. ²³ Physically, one may conceive of the raised interaction sites to correspond to polymeric ⁴⁸ or metallic ^{37–39} deposits on spherical colloids functionalized by glancing angle deposition ^{4,52,53} or contact area lithography. ³⁸

The geometry and interaction potential of the system is fully defined by the six parameters $\{\varepsilon_A, \varepsilon_B, \sigma_A, \sigma_B, \alpha_B, \phi_B\}$ defining the interaction strength, size and relative arrangement of the "A" and "B" particles. Since only the relative strength of the "A" and "B" interactions is meaningful – the absolute values can be scaled by modulating temperature – we reduce the parameter space by eliminating ε_A from consideration and considering only the relative value of ε_B . Similarly, only the relative values of σ_A and σ_B are meaningful, with the absolute values corresponding to a global rescaling in the size of the particles. In this work, we follow our previous work and fix the relative ratio of the particle size as $\sigma_A = 5\sigma_B = 5\sigma$. We achieve good results under this choice, but, in principle, we could also consider changing the size and/or shape of the patch. As such, the inverse design problem is defined over the three-dimensional design space defining the interaction strength, polar angle, and protrusion ratio of the "B" patch $\{\varepsilon_B, \phi_B, \alpha_B\}$. The design strategy seeks to optimize both the chemistry (i.e., interaction strength) and geometry (i.e., polar angle and protrusion ratio) of the anisotropic surface patches to favor the staggered dimer configuration and promote spontaneous defect-free assembly of a cubic diamond lattice.

2.3 Optimization objective function

A direct computational approach to optimizing $\{\varepsilon_B, \phi_B, \alpha_B\}$ would randomly place tetrahedral tetramers within a simulation box, gently anneal the system to induce nucleation and

growth of a crystal, and then modify $\{\varepsilon_B, \phi_B, \alpha_B\}$ to maximize yield of the cubic diamond lattice at the termination of the annealing procedure. This direct optimization is inefficient, however, due to the need for very slow cooling rates in order to avoid kinetic traps and reliably estimate the thermodynamic yield of cubic diamond crystals. ^{13,35,36} Instead, we define a proxy optimization problem in which $\{\varepsilon_B, \phi_B, \alpha_B\}$ are optimized to favor the formation of staggered dimers between colloidal monomers (i.e., isolated "A" spheres functionalized with "B" patches) at a fixed temperature. This problem is simpler and faster since we do not perform explicit slow temperature ramping during the optimization and directly focus on optimizing the colloid-colloid interface to favor an interlocking patch conformation. We show later during temperature ramping simulation for pre-assembled tetramers that transferring the optimal design found for monomeric patchy colloid to the tetrahedral tetramer does indeed result in quite high-yield cubic diamond crystals and provides post hoc validation of our more efficient proxy optimization.

We evaluate the quality of a particular $\{\varepsilon_B, \phi_B, \alpha_B\}$ triplet by conducting Langevin dynamics simulations of the assembly of colloidal monomers (Section 2.4) and computing the fraction of aggregates that exist as staggered dimers at equilibrium. We define a geometric criterion under which a dimer between colloidal monomers i and j should be classified as staggered based on the planar angle θ_{ij} and the dihedral angle Ψ_{ij} between the constituent colloids (Figure 3). The angle θ_{ij} is defined as,

$$\cos(\theta_i) = \hat{\xi}_i \cdot \hat{r}_{ij}$$

$$\cos(\theta_j) = \hat{\xi}_j \cdot \hat{r}_{ji}$$

$$\theta_{ij} = \max(\theta_i, \theta_j),$$
(3)

where $\hat{\xi}_i$ and $\hat{\xi}_j$ denote the unit orientation vectors of each particle pointing from the center of mass of the "A" colloid to the centroid of the three "B" patches and \hat{r}_{ij} denotes the unit displacement vector from i to j (Figure 3a). The planar angle θ_i measures the angle between

 $\hat{\xi}_i$ and \hat{r}_{ij} and θ_j measures the angle between $\hat{\xi}_j$ and \hat{r}_{ji} . Defining θ_{ij} as maximum of these returns the larger deviation of either partner in the dimer from a face-to-face alignment in which $\hat{\xi}_i$ and $\hat{\xi}_j$ are antiparallel.

The dihedral angle Ψ_{ij} is defined as,

$$\Psi_{ij} = \min_{m \in \text{patch}_i, n \in \text{patch}_j} (\psi_{ij}^{mn}), \tag{4}$$

where ψ_{ij}^{mn} defines the relative rotation between each of the three patches m on colloid i and the three patches n on colloid j. We compute ψ_{ij}^{mn} by finding the centroid of three patches on colloid i denoted by c_i and the centroid of three patches on colloid j denoted by c_j , then calculate ψ_{ij}^{mn} as the angle between the plane through $\{m, c_i, c_j\}$ and the plane through $\{c_i, c_j, n\}$. Denoting the vector from m to c_i as \vec{b}_1 , the vector from c_i to c_j as \vec{b}_2 , and the vector from c_j to n as \vec{b}_3 , the dihedral angle ψ_{ij}^{mn} is computed as,

$$\vec{n}_1 = \frac{\vec{b}_1 \times \vec{b}_2}{\left\| \vec{b}_1 \times \vec{b}_2 \right\|},$$

$$\vec{n}_2 = \frac{\vec{b}_2 \times \vec{b}_3}{\left\| \vec{b}_1 \times \vec{b}_2 \right\|},$$

$$\cos\left(\psi_{ij}^{mn}\right) = \vec{n}_1 \cdot \vec{n}_2.$$
(5)

The dihedral angle Ψ_{ij} is defined as the minimum over the nine ψ_{ij}^{mn} , which – assuming a small value of θ_{ij} and therefore relatively cofacial dimer alignment – quantifies the minimum rotational dihedreal between the colloids in the dimer pair required to align the patches on each colloid into an eclipsed configuration. Figure 3c provides a schematic illustration for the case in which $\Psi_{ij} = \psi_{ij}^{11'} = \psi_{ij}^{22'} = \psi_{ij}^{33'}$.

We classify a dimer as staggered if $(0^{\circ} \leq \theta_{ij} \leq 5^{\circ})$ and $(55^{\circ} \leq \Psi_{ij} \leq 60^{\circ})$. Enforcing a low threshold on θ_{ij} ensures that the patches are approximately face-to-face aligned (i.e. $\hat{\xi}_i$ and $\hat{\xi}_j$ are nearly antiparallel) and that the value of Ψ_{ij} is meaningful. An ideal staggered

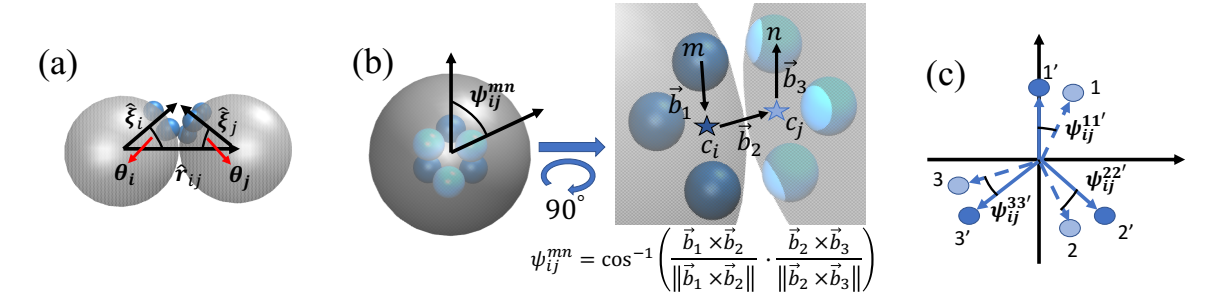


Figure 3: Geometry of self-assembled dimers of colloid monomers. (a) The angle $\theta_{ij} = \max(\theta_i, \theta_j)$ measures the larger deviation of either partner dimer i or j from a face-to-face alignment in which the unit orientation vectors $\hat{\xi}_i$ and $\hat{\xi}_j$ linking the center of the colloid to the pole containing the patch are antiparallel and collinear with the unit vector \hat{r}_{ij} linking the colloidal centers. (b) The dihedral angle Ψ_{ij} measures the minimum dihedral rotation required within a cofacial dimer pair to align the patches on each colloid into an eclipsed configuration. The value of Ψ_{ij} is taken as the minimum over all nine ψ_{ij}^{mn} defining the dihedral angles between the three patches m on colloid i and the three patches n on colloid j. The ψ_{ij}^{mn} are computed by first finding the centroid c_i of patches on colloid i and the centroid c_j of patches on colloid j and then computing the angle between the plane through $\{m, c_i, c_j\}$ (spanned by \vec{b}_1 and \vec{b}_2) and the plane through $\{c_i, c_j, n\}$ (spanned by \vec{b}_2 and \vec{b}_3). (c) Schematic diagram of $\Psi_{ij} = \min_{m \in \text{patch}_i, n \in \text{patch}_j}(\psi_{ij}^{mn})$ considering a particular interfacial arrangement of the three light blue "B" patches on colloid i and three dark blue "B" patches on colloid i. Assuming i is small such that the colloids are approximately cofacial i is i patches on colloid i defines the minimum azimuthal rotation required to achieve an eclipsed configuration.

dimer would possess ($\theta_{ij} = 0^{\circ}$, $\Psi_{ij} = 60^{\circ}$). The 5° threshold in both θ_{ij} and Ψ_{ij} is motivated by the range of the observed distribution of these angles in the ensemble of stable staggered dimers resulting from favorable $\{\varepsilon_B, \phi_B, \alpha_B\}$ choices.

Having defined a criterion by which counts the number of staggered dimers, we define the objective function to be maximized as the equilibrium fraction of staggered dimers among all self-assembled aggregates,

$$f(\varepsilon_{B}, \phi_{B}, \alpha_{B}) = \left\langle \frac{N_{\text{staggered dimer}}}{N_{\text{aggregates}}} \right\rangle$$

$$= \frac{1}{Z} \int e^{-\beta U(\boldsymbol{r}^{N}, \boldsymbol{\Omega}^{N}; \varepsilon_{B}, \phi_{B}, \alpha_{B})} \frac{N_{\text{staggered dimer}}(\boldsymbol{r}^{N}, \boldsymbol{\Omega}^{N}; \varepsilon_{B}, \phi_{B}, \alpha_{B})}{N_{\text{aggregates}}(\boldsymbol{r}^{N}, \boldsymbol{\Omega}^{N}; \varepsilon_{B}, \phi_{B}, \alpha_{B})} d\boldsymbol{\Omega}^{N} d\boldsymbol{r}^{N}$$

$$\approx \frac{1}{n} \sum_{i=1}^{n} \frac{N_{\text{staggered dimer}}(\boldsymbol{r}_{i}^{N}, \boldsymbol{\Omega}_{i}^{N}; \varepsilon_{B}, \phi_{B}, \alpha_{B})}{N_{\text{aggregates}}(\boldsymbol{r}_{i}^{N}, \boldsymbol{\Omega}_{i}^{N}; \varepsilon_{B}, \phi_{B}, \alpha_{B})}$$
(6)

where \mathbf{r}^N and $\mathbf{\Omega}^N$ denote the positions and orientations of the N patchy colloidal monomers in the simulation, \mathbf{r}_i^N and $\mathbf{\Omega}_i^N$ denote their positions and orientations in frame i of simulation

trajectory, $U(\mathbf{r}^N, \mathbf{\Omega}^N; \varepsilon_B, \phi_B, \alpha_B)$ is the potential energy of the system, $\beta = 1/k_BT$ is the reciprocal temperature, $N_{\text{staggered dimer}}$ is a function returning a count of staggered dimers according to the criterion defined above for a particular system configuration, and $N_{\text{aggregates}}$ is a function returning a count of aggregates of all sizes (monomers, staggered and non-staggered dimers, trimers, tetramers, pentamers, etc.). The ensemble average in the second line is approximated by a time-average in the third line that is evaluated over n frames from the equilibrated production portion of the Langevin dynamics simulation.

We note that the objective function defined in Equation 6 seeks to optimize the fraction of staggered dimer at equilibrium and is therefore purely thermodynamic in nature. This objective function is appropriate for self-assembling systems under thermodynamic control where the system is expected to approach its thermodynamic ground state. This can be achieved by, for example, slow temperature annealing in which case the details of the kinetic pathways and mechanisms by which self-assembly proceeds do not dictate the terminal morphologies. In systems where assembly is driven out of equilibrium such as in evaporation, sedimentation, or under the influence of external fields, an objective function accounting for the specific processing conditions must be adopted. The most straightforward choice would be to directly simulate assembly under the conditions of interest and adopt as our objective function the observed yield of the desired lattice. Direct simulation can, however, become quite expensive and requires good models for the specific details of the assembly process.

2.4 Langevin dynamics simulations

We evaluate the objective function in Equation 6 by conducting Langevin dynamics simulations of the self-assembly of patchy colloidal monomers in HOOMD-blue v2.6.0. 54,55 We initialize each simulation from a random dispersion of N=64 monomeric patchy colloids with a particular combination of $\{\varepsilon_B, \phi_B, \alpha_B\}$ design parameters and observe the distribution of self-assembled aggregates that spontaneously form. Importantly, by running many-body simulations of assembly we seek to both maximize the thermodynamic yield of the desired

staggered dimers relative to all competing aggregates and also assure their kinetic accessibility. We perform our simulation in reduced units, where $\sigma = 1$, $\varepsilon = \varepsilon_A = 1$, and m = 1. Using these units, we specify $\sigma_A = 5$, $\sigma_B = \sigma = 1$, $m_A = 125$ and $m_B = m = 1$. The relative mass of the colloid and patch is scaled in proportion to size but these choices could be tuned based on the relative densities of the colloidal "A" particle (e.g., silica, silica, polystyrene) and "B" patches (e.g., metal, polymer). We perform simulations in a cubic simulation box of side length $L = 52\sigma$, corresponding to a $\varphi = 0.05$ volume fraction of colloidal monomers. The equations of motion are numerically propagated for 1×10^8 steps using a Langevin dynamics integrator with a step size of $dt^* = 0.005$ and temperature of $T^* = 0.8$. The first 5×10^7 steps are discarded for equilibration and frames are saved every 1×10^4 steps over the remaining 5×10^7 step production period to evaluate $f(\varepsilon_B, \phi_B, \alpha_B)$ using Equation 6. We verify that the equilibration period is sufficiently long such that the system energy and aggregation numbers of various aggregates (monomers, staggered dimers, eclipsed dimers, trimers, etc.) fluctuate around stable mean values over the production period. We perform three independent simulations for each candidate and pass the mean value of the objective function to the evolutionary optimization routine (Section 2.5).

By performing the evaluation of the objective function at a single temperature of T^* = 0.8, we optimize assembly of staggered dimers at this temperature. Once the optimal design is determined, we transfer the patch design to the tetrahedral tetramers and perform slow temperature annealing from a high temperature state point at which the tetrahedral tetramers are fully dispersed to a low temperature state at which the system is fully assembled. Since ε_B is the only tunable energy scale in our reduced unit calculations, the optimal ε_B discovered at $T^* = 0.8$ may be arbitrarily rescaled to modulate the assembly temperature.

A mapping between reduced units and real units can be made by specifying the size σ_A and density ρ_A of the "A" colloid and the energy scale ε . The temperature and time in real units (T, t) are then related to corresponding quantities in reduced units (T^*, t^*) as $T = T^* \frac{\varepsilon}{k_B}$ and $t = t^* \sigma \sqrt{\frac{m}{\varepsilon}}$. For example, adopting $\sigma_A = 5\sigma = 1 \ \mu\text{m}$, $\rho_A = 1 \ \text{g/cm}^3$, and ε

= 0.4 k_BT at T=298 K means that the reduced temperature of $T^*=0.8$ corresponds to T=95 K, the reduced time step of $dt^*=0.005$ to dt=0.05 μ s, and the total length of our simulations to t=5 s.

2.5 Evolutionary optimization strategy

To minimize the simulation burden and efficiently identify optimal patch design, we numerically optimize $f(\varepsilon_B, \phi_B, \alpha_B)$ using a derivative-free evolutionary algorithm known as Covariance Matrix Adaptation Evolution Strategy (CMA-ES). ⁵⁶ We favor CMA-ES because it is robust on a large number of test functions ⁵⁷ and has demonstrated previous successes in inverse materials design. ^{9,36,58,59} Conceptually, CMA-ES updates the design parameters from one generation to the next by evaluating the fitness and distribution of a swarm of designs to form a surrogate model of the unknown objective function landscape and propose new designs that are expected to move closer to the objective function optimum. CMA-ES updates candidates from generation g to (g+1) as,

$$\boldsymbol{x}^{g+1} = \langle \boldsymbol{x}^g \rangle_{\mu} + \sigma^g \boldsymbol{\eta}^g, \tag{7}$$

where $\mathbf{x} = (\varepsilon_B, \phi_B, \alpha_B)^T$ is a column vector of design parameters, $\mathbf{\eta}^g$ is a n-dimensional random vector sampled from a multivariate Gaussian distribution with zero mean and covariance matrix C^g , σ^g is the step size and $\langle \mathbf{x}^g \rangle_{\mu}$ is the mean design vector of the top μ of the M candidates in generation g. The covariance matrix C^g and step size σ^g are updated based on the past evolution path of the top μ candidates. The covariance matrix guides the optimization towards an objective function peak and the step size modulates between broad exploration during the early generations and convergence to a point when a (local) optimum is discovered. The number of candidates per generation M and the number of top candidates μ to consider to propose the next generation are hyperparameters of the algorithm. In this work, we find M = 12 and $\mu = 3$ to provide a good balance between computational cost per

generation and efficient exploration of design space. We terminate the optimization when when the standard deviations in $\{\varepsilon_B, \phi_B, \alpha_B\}$ simultaneously fall below $\{0.33\varepsilon, 1.0^\circ, 0.01\}$. These thresholds are selected to ensure a tight optimum in the terminal design and may be tuned based on the experimental precision with which these parameters may be controlled. A flow diagram of the optimization procedure is shown in Figure 4.

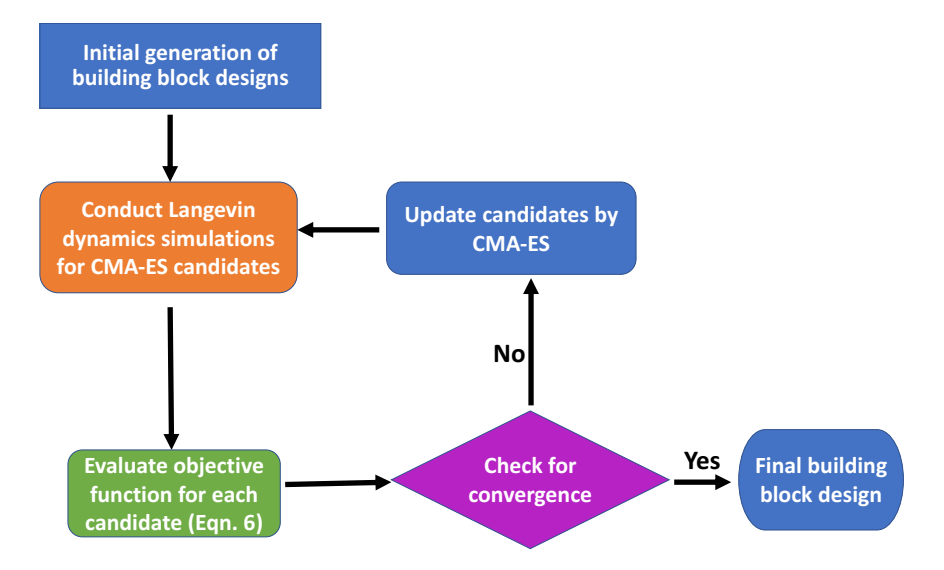


Figure 4: Flow diagram of the optimization procedure combining Covariance Matrix Adaptation Evolution Strategy (CMA-ES) and Langevin dynamics simulations.

3 Results and discussion

We first report the determination of the optimal patch parameters determined using our CMA-ES optimization and Langevin dynamics protocol to maximally favor the assembly of staggered dimers of colloidal monomers. We then transfer this patch design to tetrahedral tetramers and report our validation of their capacity to assemble into a cubic diamond lattice in slow temperature annealing simulations.

3.1 Determination of optimal patch design

We commenced the optimization loop in Figure 4 by seeding it with M=12 initial building block designs with parameters $\{\varepsilon_B, \phi_B, \alpha_B\}$ sampled from a multivariate Gaussian distribution with mean $\langle \boldsymbol{x}^0 \rangle = (3.33\varepsilon, 20.00^\circ, 0.85)^T$ and covariance $C^0 = \text{diag}(1.11, 10.00, 0.01)$. Hereafter, we call each particular set of parameters $\{\varepsilon_B, \phi_B, \alpha_B\}$ a "candidate" in the parameter space. The initial step size was set to $\sigma^0 = 1.0$ to favor early exploration of the design space and mitigate possible trapping in a local optimum. It is our experience that the CMA-ES optimization can robustly converge to optimal solutions even for poor initial building block designs and sub-optimal hyperparameter choices. ^{9,36} For each candidate, we ran three independent Langevin dynamics simulations and passed the average of the objective function value (Equation 6) obtained from each simulation to the optimizer. Subsequent CMA-ES generations were seeded based on the top $\mu=3$ of the M=12 candidates (Equation 7).

The evolution of $\{\varepsilon_B, \phi_B, \alpha_B\}$ over the course of CMA-ES generations are presented in Figure 5a-c and the evolution of the mean value of objective function over the top $\mu=3$ candidates for each generation is shown in Figure 5d. In conducting the optimization we constrained the protrusion ratio to lie in the range $\alpha_B=[0.8,1.0]$ by penalizing the objective function to $f=(-\infty)$ for candidates outside of this range. This prevented the aphysical situations of the patch detaching from the colloid $(\alpha_B>1.0)$ or completely sinking below the surface $(\alpha_B<(1-\sigma_B/\sigma_A)=0.8)$. The optimizer converges to a value of α_B inside this range and these constraints are inactive in the later generations of the optimization. The optimization is terminated at generation g=28 at which point the standard deviations $\{0.239\varepsilon, 0.300^\circ, 0.005\}$ in the three design variables proposed for generation g=29 fall below the prescribed convergence thresholds of $\{0.33\varepsilon, 1.0^\circ, 0.01\}$ and the mean design is declared the converged solution $\{\varepsilon_B^{\rm opt}, \phi_B^{\rm opt}, \alpha_B^{\rm opt}\} = \{8.18\varepsilon, 19.6^\circ, 0.907\}$. Under the reduced to real unit mapping defined in Section 2.4, the optimal interaction strength corresponds in real units to $\varepsilon_B^{\rm opt}=3.3$ k_BT at T=298 K.

Inspection of the optimization time courses show that the interaction strength ε_B climbs

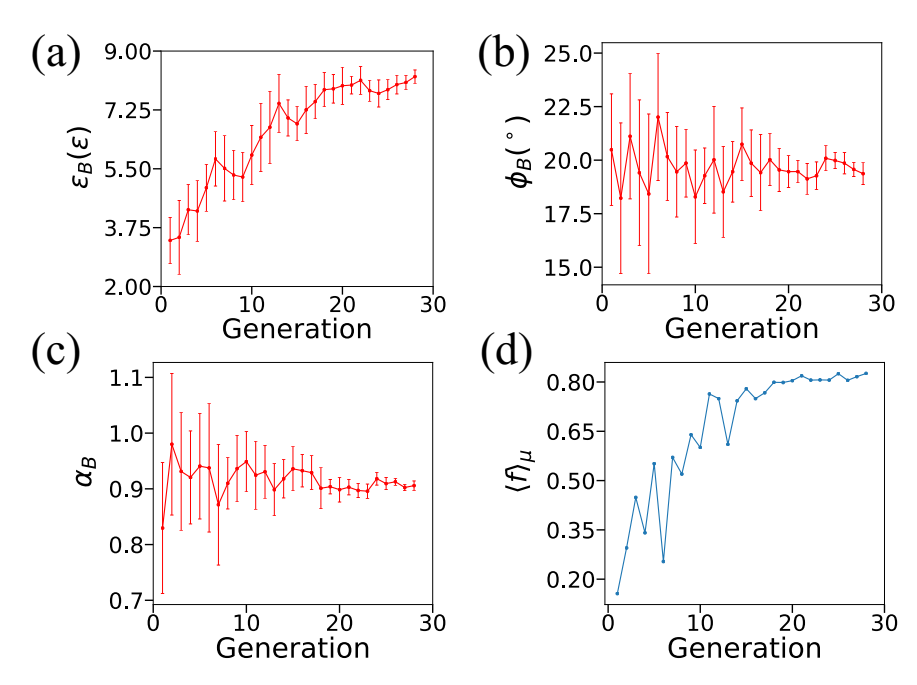


Figure 5: Evolution of design parameters and objective function over the CMA-ES optimization course. Evolution of the (a) interaction strength ε_B , (b) polar angle ϕ_B , and (c) protrusion ratio α_B over the 28-generation optimization. The lines and error bars correspond, respectively, to the mean and standard deviation of each parameter over the M=12 candidates in each generation. The optimization converges at generation g=28 to an optimum of $\{\varepsilon_B^{\rm opt},\phi_B^{\rm opt},\alpha_B^{\rm opt}\}=\{8.18\varepsilon,19.6^{\circ},0.907\}$. (d) The mean value of objective function (Equation 6) evaluated over the top $\mu=3$ candidates in each generation reporting the fraction of staggered dimers among self-assembled aggregates. The terminal value of the mean objective function value reaches $\langle f^{28} \rangle_{\mu}=0.83$ corresponding to 83% staggered dimers.

from its initial starting point of 3.33 ε to more than double and reach its terminal plateau at 8.18 ε by around generation g=20 (Figure 5a). The protrusion ratio α_B undergoes some exploratory fluctuations before increasing slightly from it starting point of 0.85 to settle down to its terminal optimum of 0.907 (Figure 5c). The polar angle ϕ_B reaches an optimum of 19.6° that is changed very little from the initial guess of 20.0°, but the large fluctuations in the early generations show that the algorithm does broadly explore a variety of angles before converging (Figure 5b). The mean value of objective function evaluated over the top $\mu=3$ candidates undergoes large fluctuations in the early generations but by generation g=15 approaches and then asymptotes to a high plateau that nearly quintuples the fraction staggered dimers among aggregates from $\langle f^0 \rangle_{\mu}=0.17$ to $\langle f^{28} \rangle_{\mu}=0.83$.

Analysis of the assembly trajectories allow us to rationalize the behavior of the optimizer from a structural perspective. The polar angle ϕ_B is constrained to lie in the vicinity of 20° in order to admit interlocked colloidal interfaces between the tetrahedral tetramers (Figure 2). At this angle, the patches can maximize favorable contacts via short range attractive Lennard-Jones interactions (Equation 1) in an interlocked configuration wherein each patch interacts with two nearest neighbors. Smaller angles prevent a tight interlocking due to insufficient free volume between the patches and lager angles spread the patches too far apart to admit two nearest neighbor contacts. Larger protrusion ratios α_B and stronger interaction strengths ε_B would appear to offer increasing energetic stabilization of the staggered dimer but this process must be viewed in the context of alternative accessible assembly pathways and states. This process is limited by the fact that too large protrusion ratios and interaction strengths make the triplet of "B" patches too accessible and strongly bound to multiple interaction partners, thereby favoring the formation of large aggregates that can outcompete the staggered dimer. Furthermore, the interaction strength cannot be so strong as to prevent mutual rearrangements and relaxations of bound particles thereby preventing irreversible aggregation and kinetic trapping into a glass. ⁶⁰

3.2 Validation of optimal patch design

The optimal patch design programs 83% of colloidal monomers to assemble into staggered dimers. We now proceed to validate that this same patch design can also induce the robust assembly of tetrahedral tetramers into a cubic diamond lattice.

3.2.1 Slow temperature annealing assembly of optimal tetrahedral tetramers

We conduct Langevin dynamics simulations of N = 512 initially randomly placed tetrahedral tetramers decorated with the optimal patch design $\{\varepsilon_B^{\text{opt}}, \phi_B^{\text{opt}}, \alpha_B^{\text{opt}}\} = \{8.18\varepsilon, 19.6^\circ, 0.907\}$. We recall that these tetrahedral tetramers comprise a rigid cluster of four "A" colloids each decorated with three "B" patches as a simplified model of an experimentally-realizable "colloidal molecule" $^{40-43,46,47}$ functionalized by surface patterning techniques to induce anisotropic patchy interactions. 37-39,48 Simulations were conducted in a cubic box with side length $L=204.08\sigma$, corresponding to a tetrahedral tetramer volume fraction of $\varphi=0.05$. We perform a high-temperature equilibration of the system at $T_{\text{high}}^* = 4.0 \ (T_{\text{high}} = 476.8 \ \text{K},$ under the real unit mapping defined in Section 2.4) for 1×10^8 steps with a step size of $dt^* = 0.005$ ($t^* = 5 \times 10^5$; t = 5.0 s). Under these high temperature conditions the attractive "B" patch interactions are insufficient to promote aggregation and the tetrahedral tetramers behave effectively as an ideal gas. We then perform slow temperature annealing of the system under a linear ramp down to $T_{\mathrm{low}}^* = 2.0~(T_{\mathrm{low}} = 238.4~\mathrm{K})$ over the course of 2×10^9 steps ($t^*=1\times 10^7;\;t=101$ s; $\Delta T/t=2.36$ K/s). Finally, we conduct a 1×10^7 step (t^* $=5 imes 10^4;~t=0.5$ s) hold at $T_{
m low}^*=2.0~(T_{
m low}=238.4$ K) over which we collect data on the self-assembled structure. The complete 2.11×10^9 step simulation protocol is conducted using HOOMD-blue^{54,55} and executes in 4 GPU-days on a NVIDIA TITAN V GPU card.

The plots of temperature and potential energy over the course of the annealing run are presented in Figure 6. The system undergoes an assembly transition from the initial dispersion of isolated tetrahedral tetramers marked by the precipitous drop in potential energy at $t^* \approx 0.7 \times 10^7$ (Figure 6b) corresponding to a temperature of $T^* \approx 2.75$ (Figure

6a). The small temperature peak in Figure 6a at $t^* \approx 0.7 \times 10^7$ can be attributed to the latent heat of fusion released upon assembly. A slow cooling schedule was adopted to favor a single nucleation event of the most thermodynamically favored polymorph and avoid kinetic traps. Assembly commences at a higher temperature $(T^* \approx 2.75)$ than that at which the patch design was optimized $(T^* = 0.8)$, indicating that the optimization of the patches was conducted well below the phase boundary for assembly. As detailed above, regardless of the temperature at which the optimization was conducted, the transition temperature may be tuned by rescaling $\varepsilon_B^{\text{opt}}$.

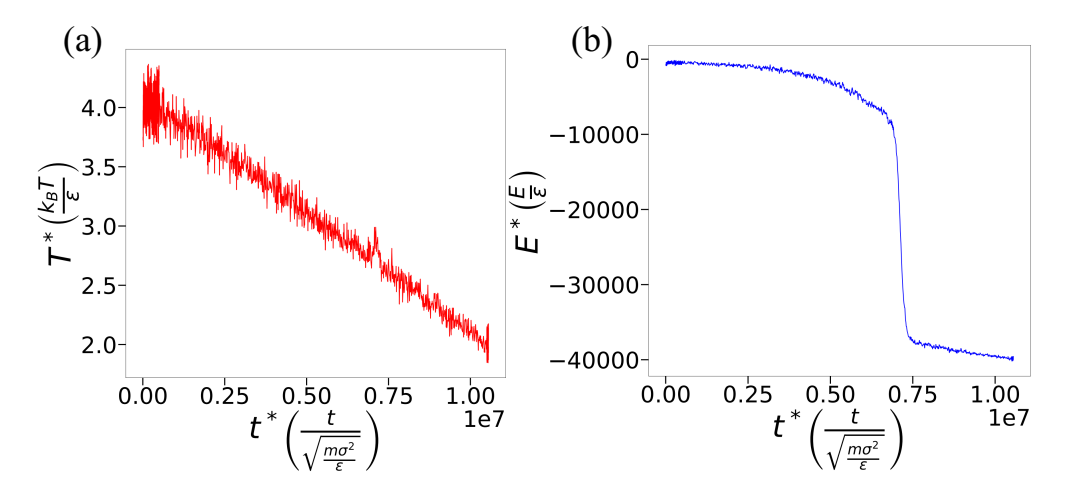


Figure 6: Slow temperature annealing induction of tetrahedral tetramer self-assembly. (a) Commencing from an equilibrated high-temperature effective ideal gas of tetrahedral tetramers at $T_{\rm high}^* = 4.0$, a linear temperature ramp down to $T_{\rm low}^* = 2.0$ is executed over the course of 2×10^9 integration steps of $dt^* = 0.005$. (b) The potential energy over the course of the cooling run undergoes a precipitous drop at $t^* \approx 0.7 \times 10^7$ corresponding to a temperature of $T^* \approx 2.75$ that marks the assembly transition. The small temperature spike at $t^* \approx 0.7 \times 10^7$ is attributable to the latent heat of fusion released by the self-assembly process.

3.2.2 Characterization of the self-assembled lattice

We now analyze the structure of the self-assembled lattice produced in the slow temperature annealing to assess the yield of the desired cubic diamond lattice. The self-assembled crystal produced at the end of the low temperature hold is presented in Figure 7a. We characterize the structure by computing the radial distribution function of the geometric centers of tetramers (Figure 7b) and the inner product of the Steinhardt bond-order parameters ^{61,62}

 $\vec{q_3}(i)^* \cdot \vec{q_3}(j)$ between nearest-neighbor pairs of geometric centers of tetramers, where the asterisk denotes the complex-conjugate (Figure 7c). The (non-normalized) vector $\vec{q_l}(i)$ is a (2l+1)-dimensional vector with components,

$$q_{lm}(i) = \frac{1}{N_b(i)} \sum_{k=1}^{N_b(i)} Y_{lm}(\hat{r}_{ik}) = \frac{1}{N_b(i)} \sum_{k=1}^{N_b(i)} Y_{lm}(\theta_{ik}, \phi_{ik}), \tag{8}$$

where k loops over the $N_b(i)$ nearest neighbors of particle i, \hat{r}_{ik} is the unit displacement vector from particle i to k, $\{\theta_{ik}, \phi_{ik}\}$ are the polar and azimuthal angles defined by \hat{r}_{ik} with respect to a pre-defined coordinate system, and Y_{lm} are spherical harmonics with order l and degree m where $|m| \leq l$. It can be shown that the inner product between any two vectors $\vec{q}_i(i)^* \cdot \vec{q}_i(j)$ is real and independent of coordinate system. ^{61,62} Nearest-neighbors are defined according to a cut-off distance $d_{cut} = 12.0\sigma$ covering the first peak in the radial distribution function.

The radial distribution function shows sharp peaks at $r^* = 11.25\sigma$, 18.45σ , 21.55σ , 26.05σ and 28.35σ corresponding to the locations of the first five characteristic peaks expected for a cubic diamond lattice (Figure 7b). The hexagonal diamond lattice, however, possesses a nearly indistinguishable peak fingerprint that differs only in a weak splitting of the second and fourth peaks. Instead we turn to the $\vec{q_3}(i)^* \cdot \vec{q_3}(j)$ Steinhardt bond-order parameter analysis that is better able to distinguish these two polymorphs by also incorporating angular information. ^{6,36} The distribution of $\vec{q_3}(i)^* \cdot \vec{q_3}(j)$ computed over all nearest-neighbor pairs (Figure 7c) exhibits a strong primary peak at (-1) and a smaller peak at (-0.115). The additional peaks between (-1) and (-0.115) are attributable to finite-size effects due to computing $\vec{q_3}(i)^* \cdot \vec{q_3}(j)$ over tetramers on the boundary of the final structure that do not possess exactly four nearest-neighbors. Excluding these boundary particles by restricting the calculation to nearest-neighbor pairs possessing exactly four nearest-neighbors eliminates these ancillary peaks (Figure 7d). An ideal cubic diamond lattice should possess a single peak in $\vec{q_3}(i)^* \cdot \vec{q_3}(j)$ at (-1). A hexagonal diamond lattice should possess an additional peak at

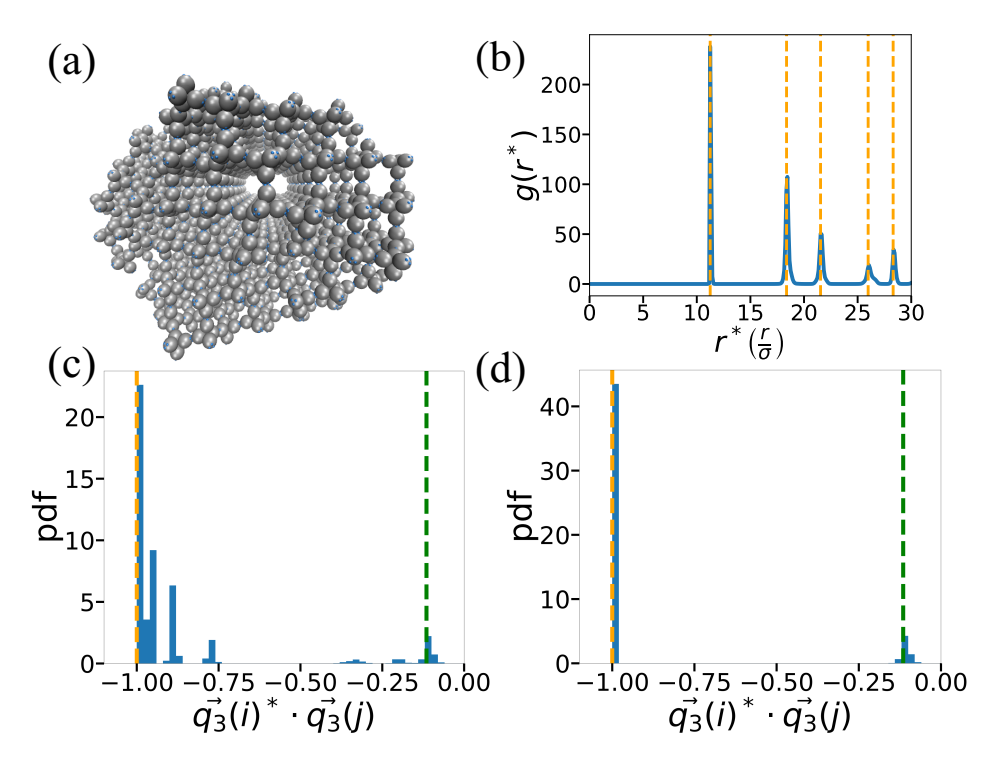


Figure 7: Characterization of the self-assembled crystal lattice. (a) A snapshot of the terminal self-assembled lattice. (b) Radial distribution function of the geometric centers of tetramers in the terminal lattice. The orange dashed lines correspond to characteristic peak positions of an ideal cubic diamond lattice. (c) Distribution of the inner product of Steinhardt bond-order parameters $\vec{q_3}(i)^* \cdot \vec{q_3}(j)$ between nearest-neighbor pairs of geometric centers of tetramers. The orange dashed line corresponds to the characteristic peak of cubic diamond lattice and the green dashed line corresponds to the extra peak in hexagonal diamond lattice. (d) Reproduction of panel c considering only tetramers possessing four nearest neighbors to exclude tetramers at the boundary of the finite-sized crystal.

(-0.115) with a magnitude one third of that of the (-1) peak.⁶

We quantify the proportions of tetrahedral tetramers within cubic and hexagonal diamond environments following an approach suggested by Romano et al. ⁶ First, we classify a tetramer i as solid-like if it has four nearest neighbors with $\vec{q_3}(i)^* \cdot \vec{q_3}(j) \in [-1, -0.87) \cup [-0.3, 0.1)$ where the former range identifies cubic diamond neighbors and the latter range hexagonal diamond neighbors – and each of its nearest neighbors also has four nearest neighbors. Second, we classify a solid-like tetramer i as living in a cubic diamond environment if $\vec{q_3}(i)^* \cdot \vec{q_3}(j) \in [-1, -0.87)$ for all four neighbors j. To provide a statistical estimate of these fractions, we performed 10 independent temperature annealing simulations using the method described at the beginning of this section and measured the fraction of solid-like tetramers

living in a cubic diamond environment in self-assembled crystal at the termination of the low-temperature hold. We compute a mean cubic diamond fraction of 58% with a 95% confidence interval of (53%, 63%).

The root of the mixed cubic/hexagonal character of the self-assembled lattice is the small free energy difference between the two polymorphs. A short-ranged attractive model of tetramers developed by Romano et al. calculated the cubic phase to be only marginally more stable than the hexagonal phase by only $0.02~k_BT$ in a short-range patchy particle model. In analogous work, triblock patchy colloids designed by Rao et al. were observed to form a mixed pyrochlore/hexagonal tetrastack lattice upon slow temperature annealing as a result of a similarly marginal stability of the pyrochlore polymorph. In the present work, we sought to break the degeneracy between the desired cubic diamond polymorph relative to the undesired hexagonal diamond by engineering the geometry and interactions of the three "B" patches to favor a staggered interface between tetrahedral tetramers over the eclipsed. Although we were able to achieve 83% selectivity for the formation of staggered dimers over all competing aggregates in our simulations of colloidal monomer aggregation, this only translated to a 58% selectivity for the cubic diamond under our temperature annealing protocol.

3.2.3 Boosting the cubic diamond fraction

We experimented with a number of ways to boost the cubic diamond fraction of the self-assembled lattice. First, we explored the sensitivity of the observed cubic diamond fraction to modifications of the patch size σ_B . In prior work, we observed good assembly behaviors at a particle to patch ratio of $\sigma_A = 5\sigma_B = 5\sigma$, motivating us to fix $\sigma_B = 1.0\sigma$ and not include it within our patch optimization protocol.³⁶ It is, however, valuable to assess the robustness of our optimal design to variations in patch size and we also reasoned that small changes could potentially elevate the cubic diamond fraction. Following the same cooling schedule described in Section 3.2.1, we measured the fraction of solid-like tetramers in a cubic diamond

environment for self-assembled crystals produced by our optimal particle design but now with patch sizes of $\sigma_B = 0.90\sigma$, 0.95σ , 1.05σ , 1.10σ , 1.20σ , 1.30σ and 1.40σ . For each σ_B , we performed three independent cooling simulations. The resulting cubic diamond fractions with 95% confidence intervals for those patch sizes are illustrated in Figure 8. Within the error bars of our calculations, the observed selectivity for cubic diamond is robust to variations in the patch size over the range $\sigma_B = 0.95\text{-}1.20\sigma$. A degradation in the observed fraction is observed outside this range at $\sigma_B = 0.90\sigma$, 1.30σ , and 1.40σ . This result indicates that our optimal design lies within a relatively flat-topped optimum with respect to perturbations in σ_B and provides post hoc validation that fixing $\sigma_B = 1.0\sigma$ produces good assembly behaviors. It is conceivable that augmenting our design space to explicitly include σ_B could potentially open up directions in the 4D space of $\{\varepsilon_B, \phi_B, \alpha_B, \sigma_B\}$ along which significant improvements in the cubic diamond fraction might be observed, but the present result indicates that this cannot be achieved by modulating σ_B alone.

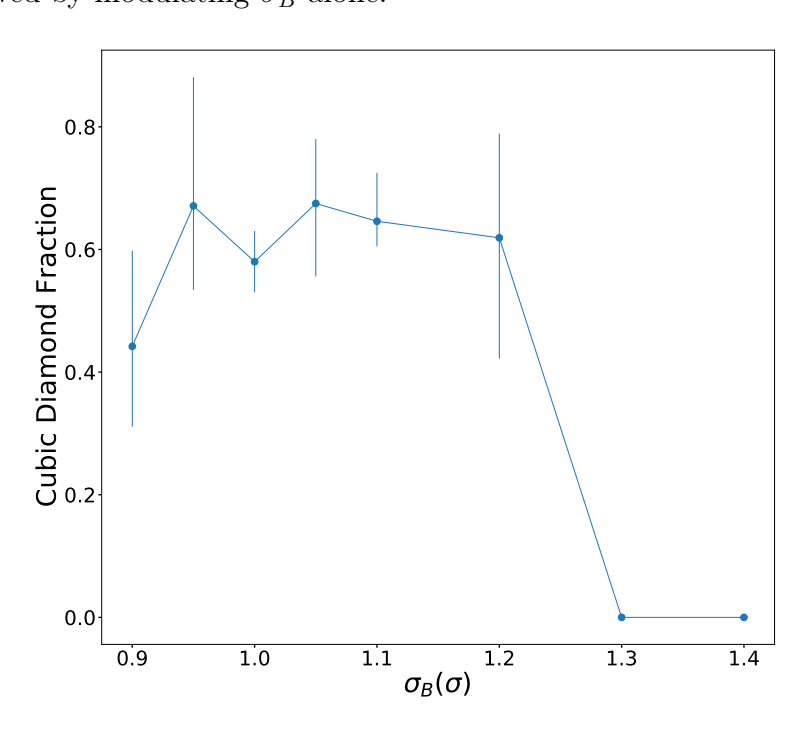


Figure 8: Sensitivity to patch size σ_B of the observed cubic diamond fraction produced by the optimal particle design $\{\varepsilon_B^{\rm opt},\phi_B^{\rm opt},\alpha_B^{\rm opt}\}=\{8.18\varepsilon,19.6^\circ,0.907\}$ after slow temperature annealing. The selectivity for cubic diamond within the self-assembled crystal is robust to perturbations in the patch size over the range $\sigma_B=0.95\text{-}1.20\sigma$. Error bars represent 95% confidence intervals.

Second, we explored the use of cubic diamond seeds to promote nucleation of the desired polymorph. Specifically, we introduced a small rigid seed of cubic diamond lattice composed of 18 tetrahedral tetramers, performed 10 independent cooling simulations for the seeded system using the same cooling schedule. This proved to be a quite successful strategy, with the cubic diamond fraction of the terminal crystal in the seeded system achieving 82% with a 95% confidence interval of (74%, 89%). Third, we explored changing the temperature annealing rate in the absence of a cubic diamond seed. There exist multiple examples in the literature demonstrating that slow cooling rates can improve the quality of self-assembled colloidal crystals.^{7,13,35} By doubling the length of the annealing schedule (i.e., halving the cooling rate) to anneal the system from $T_{\rm high}^*=4.0$ to $T_{\rm low}^*=2.0$ over 4×10^9 steps (t^* = 2×10^7 ; t = 202 s; $\Delta T/t = 1.18$ K/s), we achieved a fraction of solid-like tetramers in cubic diamond environment of 72%. (Due to the excessive computational cost, we only performed one such simulation.) Further extending the annealing period quickly becomes computationally prohibitive, but we performed cooling simulations at three additional shorter annealing periods: 5×10^8 steps $(t^* = 2.5 \times 10^6; t = 25.2s; \Delta T/t = 9.45 \text{ K/s}), 1 \times 10^9 \text{ steps}$ $(t^* = 5 \times 10^6; t = 50.5 \text{ s}; \Delta T/t = 4.73 \text{ K/s}) \text{ and } 1.5 \times 10^9 \text{ steps } (t^* = 7.5 \times 10^6; t = 75.7s; t =$ $\Delta T/t = 3.15 \text{ K/s}$). A least squares linear regression on the observed cubic diamond fractions at each of these five cooling schedules as a function of t^* admits a robust linear fit (R^2 0.99), and a subsequent linear extrapolation estimates that a perfect cubic diamond lattice may be achieved by annealing over 8.4×10^9 steps ($t^* = 4.2 \times 10^7$; t = 423.8s; $\Delta T/t = 0.56$ K/s).

The observations from our seeding and cooling runs are very promising in suggesting that a combination of slow annealing and initial seeding may be combined to exploit the small separation in the stability of the cubic over hexagonal polymorphs introduced by our patch design to induce the assembly of defect-free cubic diamond lattices. We note that we also experimented with the addition of screened dipole-dipole interactions between colloids to enhance the energy gap between the staggered and eclipsed configurations using

electrostatic interactions as suggested by Zhang et al. ¹³ We found, however, that this strategy – at least for the present design – does not work because the strength of the dipole-dipole interaction required to break the degeneracy between the two configurations was so strong as to completely destabilize the formation of dimers in the first place.

3.2.4 Band structure calculation

Finally, we compute the band structure of an ideal cubic diamond lattice formed by our designed tetrahedral tetramers. This calculation verifies that the patches do not disrupt the band structure of the underlying cubic diamond lattice of tetrahedral tetramers and that if a defect-free crystal lattice of these particles can be achieved, it will possess a complete band gap. We used the MIT Photonic Bands (MPB) package 63 to compute the band diagram along the corners of the irreducible region of the first Brillouin zone employing a $16 \times 16 \times 10^{-5}$ 16 grid to discretize the unit cell. For the cubic diamond lattice composed of tetramers, the lattice constant a is related to the nearest neighbor distance between colloids $r_{\rm nn}$ by $a=(2\sqrt{2}+\frac{4}{3}\sqrt{3})r_{\rm nn}$. We set $r_{\rm nn}=5.05\sigma$, corresponding to the first peak of the radial distribution function between patchy colloids ("A" particles) in the final structure. Assuming a relative permittivity between the colloidal particles and the medium of ϵ_r 12.0 corresponding to that between silicon and air, we compute the band structure in Figure 9a. The cubic diamond lattice does indeed possess a complete photonic band gap between the second and third bands with a ratio between gap size and midgap frequency of $\Delta\omega/\omega_m$ = 13.8%. Under the real unit mapping described in Section 2.4 with $\sigma_A = 5\sigma = 1~\mu\text{m}$, the corresponding lattice constant of $a = 5.2 \mu m$ places the band gap in the frequency range $39 < \nu < 45$ THz and wavelength range of 6.7 $\mu \rm m < \lambda < 7.7~\mu m,$ situating the band gap around the near-infrared regime of the electromagnetic spectrum.

We performed a corresponding calculation for the ideal hexagonal diamond lattice in which the lattice constant a is related to $r_{\rm nn}$ as $a = (2 + \frac{2}{3}\sqrt{6})r_{\rm nn}$. The resulting band structure assuming the same silicon/air relative permittivity of $\epsilon_r = 12.0$ is presented in

Figure 9b. At this relative permittivity, the hexagonal diamond lattice does not possess a complete photonic band gap. By examining the band structure as a function of relative permittivity, the hexagonal diamond lattice does support a complete band gap between the fourth and fifth bands, but the band only opens for relative permittivity in excess of ϵ_r = 14.0, corresponding to the approximate relative permittivity between silicon-germanium alloy and air (Figure 9c). The cubic diamond lattice possesses a substantially larger ratio between gap size and midgap frequency $\Delta\omega/\omega_m$ at all values of ϵ_r , making the cubic diamond a more attractive photonic crystal than the hexagonal analogue.

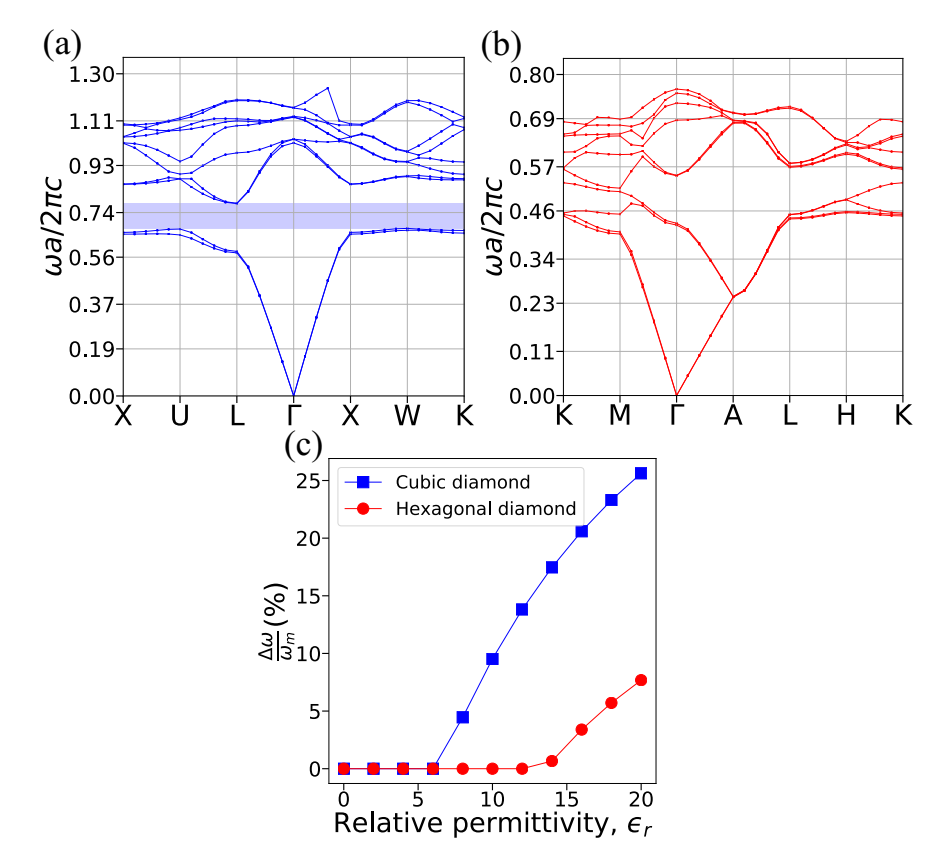


Figure 9: Photonic band structure of diamond lattices of the designed tetrahedral tetramers. (a) Computed photonic band diagram for the cubic diamond lattice of tetrahedral tetramers at a relative permittivity between the colloidal particles and the medium of $\epsilon_r = 12.0$. The x-axis traverses the corners of irreducible region in the first Brillouin zone. The y-axis reports the dimensionless frequency $\omega a/2\pi c$, where ω is the angular frequency, a is the lattice constant, and c is the speed of light in vacuum. The shaded bar denotes the complete band gap between the second and the third bands. (b) Computed photonic band diagram for the hexagonal diamond lattice of tetrahedral tetramers at $\epsilon_r = 12.0$. (c) Dependence of the ratio between gap size $\Delta \omega$ and midgap frequency ω_m as a function of relative permittivity ϵ_r for the cubic and hexagonal diamond lattices.

4 Conclusions

We have performed inverse design of a patchy tetrahedral colloidal cluster that spontaneously assembles into a cubic diamond lattice with high fidelity. We stabilize the open lattice structure through the geometry and anisotropic interaction potentials of the colloidal cluster building blocks and promote the cubic diamond polymorph over the competing hexagonal diamond by rational engineering of the strength, positioning, and protrusion of the interaction patches through an iterative optimization strategy. We have previously reported a patchy spherical colloidal building block comprising nine patches of three different types and interaction complementarities that was capable of defect-free assembly into a cubic diamond lattice in slow cooling simulations. ³⁶ In this work, we greatly simplified the design space to a single interaction patch type upon a tetrahedral colloidal cluster that is more representative of experimentally realizable designs and amenable to existing experimental fabrication techniques. Colloidal clusters, including the tetrahedral tetramer, have been produced by a variety of experimental techniques, 43 including controlled surface-nucleation of colloids onto seeds, ⁶⁴ advanced encapsulation emulsion techniques, ^{10,42,65} depletion interactions ⁴⁰ and crystal-templated fabrication. 41 Anisotropic interaction patches can be functionalized onto colloids using techniques such as contact area lithography, 37-39 glancing angle deposition, 4,52,53 grafting of DNA oligomers 10,22,66-68 and surface-patterning with polymeric or metallic patches. 48 We demonstrated the assembly of a cubic diamond lattice with 82% yield using seeded slow temperature annealing simulations of our optimal design, and our calculations suggest that even slower cooling rates can achieve defect-free assembly. The ideal cubic diamond lattice composed of these colloidal particles was computationally verified to possess a complete photonic band gap. It is hoped that this computational work may guide the experimental fabrication of self-assembling building blocks to realize this material in the laboratory.

We see multiple avenues for potential future work. First, we would like to expand the design space to incorporate additional design variables within the optimization that may

further promote robust assembly of the target cubic diamond lattice. The present work defined a three-dimensional optimization problem in the interaction strength, polar angle, and protrusion ratio of the surface patches, but the design strategy could be straightforwardly extended to include, for example, the size and shape of the patches to explore larger, smaller, and potentially non-spherical geometries. One might also allow for more elaborate expansions of the design space such as allowing for potentially non-isotropic patch interactions, 26 deviations from the idealized tetrahedral tetramer geometry to a compressed or other imperfect geometries, ²³ or changes in the surface chemistry and interaction of the colloids to mimic, for example, polymer adsorption and depletion effects. ⁶⁹ Second, the present study can be conceived as defining the single optimal patch design within the defined design space. Determining the influence of polydispersity in the design of the colloidal particles is important in understanding its impact on assembly fidelity and placing bounds on acceptable variabilities and imperfections in particle synthesis. We envisage a comprehensive follow-on study on the influence of polydispersity in the optimizable (i.e., patch interaction strength, polar angle, and protrusion ratio) and fixed (e.g., patch size, shape, and interaction strength; size, shape, and relative arrangement of the colloids comprising the tetrahedral tetramer) design variables in which we conduct ensembles of additional simulated annealing calculations to sample this multidimensional parameter space and explore these effects. One could also conceive of a more sophisticated design strategy where the optimization is performed such that the particle design parameters are random variables drawn from pre-defined distributions representing the anticipated polydispersity. 70 The terminal designs discovered by this strategy are likely to be inferior in assembly performance relative to the single best design discovered in the absence of polydispersity, but superior in terms of robustness to imperfections in the particle designs. Third, the interaction potentials adopted in this work represent simplified and idealized models that distill the essential physics of the colloid-colloid interactions. Reducing these designs to experimental practice would be well served by considering more realistic interaction potentials appropriate to particular surface functionalizations by, for example,

polymers, ⁶⁹ metals, ⁷¹ or complementary DNA oligomers. ^{10,12} Finally, we see broad applications for our simple and generic design strategy for the design of colloidal, nanoparticle, and peptide building blocks for the assembly of diverse self-assembling aggregates and materials.

Acknowledgement

This material is based upon work supported by the National Science Foundation under Grant No. DMR-1841800. We gratefully acknowledge computing time on the University of Chicago high-performance GPU-based cyberinfrastructure supported by the National Science Foundation under Grant No. DMR-1828629.

References

- (1) Zhang, Z.; Glotzer, S. C. Self-Assembly of Patchy Particles. *Nano Letters* **2004**, *4*, 1407–1413.
- (2) Wilber, A. W.; Doye, J. P. K.; Louis, A. A.; Noya, E. G.; Miller, M. A.; Wong, P. Reversible self-assembly of patchy particles into monodisperse icosahedral clusters. *The Journal of Chemical Physics* 2007, 127, 085106.
- (3) Williamson, A. J.; Wilber, A. W.; Doye, J. P. K.; Louis, A. A. Templated self-assembly of patchy particles. *Soft Matter* **2011**, *7*, 3423–3431.
- (4) Chen, Q.; Bae, S. C.; Granick, S. Directed self-assembly of a colloidal kagome lattice.

 Nature 2011, 469, 381–384.
- (5) Pattabhiraman, H.; Avvisati, G.; Dijkstra, M. Novel pyrochlorelike crystal with a photonic band gap self-assembled using colloids with a simple interaction potential. *Phys. Rev. Lett.* 2017, 119, 157401.
- (6) Romano, F.; Sanz, E.; Sciortino, F. Crystallization of tetrahedral patchy particles in silico. *The Journal of Chemical Physics* **2011**, *134*, 174502.
- (7) Morphew, D.; Shaw, J.; Avins, C.; Chakrabarti, D. Programming hierarchical self-assembly of patchy particles into colloidal crystals via colloidal molecules. *ACS Nano* **2018**, *12*, 2355–2364.
- (8) Long, A. W.; Ferguson, A. L. Nonlinear machine learning of patchy colloid self-assembly pathways and mechanisms. *The Journal of Physical Chemistry B* **2014**, *118*, 4228–4244.
- (9) Long, A. W.; Ferguson, A. L. Rational design of patchy colloids via landscape engineering. *Molecular Systems Design & Engineering* **2018**, *3*, 49–65.
- (10) Ducrot, É.; He, M.; Yi, G.-R.; Pine, D. J. Colloidal alloys with preassembled clusters and spheres. *Nature Materials* **2017**, *16*, 652–657.

- (11) Mahynski, N. A.; Rovigatti, L.; Likos, C. N.; Panagiotopoulos, A. Z. Bottom-up colloidal crystal assembly with a twist. *ACS Nano* **2016**, *10*, 5459–5467.
- (12) Wang, Y.; Jenkins, I. C.; McGinley, J. T.; Sinno, T.; Crocker, J. C. Colloidal crystals with diamond symmetry at optical lengthscales. *Nature Communications* **2017**, *8*, 14173.
- (13) Zhang, Z.; Keys, A. S.; Chen, T.; Glotzer, S. C. Self-assembly of patchy particles into diamond structures through molecular mimicry. *Langmuir* **2005**, *21*, 11547–11551.
- (14) Garcia-Adeva, A. Band gap atlas for photonic crystals having the symmetry of the kagomé and pyrochlore lattices. *New Journal of Physics* **2006**, *8*, 86–86.
- (15) Ducrot, E.; Gales, J.; Yi, G.-R.; Pine, D. J. Pyrochlore lattice, self-assembly and photonic band gap optimizations. *Optics Express* **2018**, *26*, 30052–30060.
- (16) González-Urbina, L.; Baert, K.; Kolaric, B.; Pérez-Moreno, J.; Clays, K. Linear and nonlinear optical properties of colloidal photonic crystals. *Chemical Reviews* 2012, 112, 2268–2285.
- (17) Hynninen, A.-P.; Thijssen, J. H. J.; Vermolen, E. C. M.; Dijkstra, M.; van Blaaderen, A. Self-assembly route for photonic crystals with a bandgap in the visible region. *Nature Materials* **2007**, *6*, 202–205.
- (18) Ngo, T. T.; Liddell, C. M.; Ghebrebrhan, M.; Joannopoulos, J. D. Tetrastack: Colloidal diamond-inspired structure with omnidirectional photonic band gap for low refractive index contrast. Applied Physics Letters 2006, 88, 241920.
- (19) Lončar, M.; Doll, T.; Vučković, J.; Scherer, A. Design and fabrication of silicon photonic crystal optical waveguides. *Journal of Lightwave Technology* **2000**, *18*, 1402.
- (20) Joannopoulos, J.; Johnson, S.; Winn, J.; Meade, R. *Photonic Crystals: Molding the Flow of Light Second Edition*; Princeton University Press: Princeton, U.S., 2011.

- (21) Maldovan, M.; Thomas, E. L. Diamond-structured photonic crystals. *Nature Materials* **2004**, *3*, 593.
- (22) Liu, W.; Tagawa, M.; Xin, H. L.; Wang, T.; Emamy, H.; Li, H.; Yager, K. G.; Starr, F. W.; Tkachenko, A. V.; Gang, O. Diamond family of nanoparticle superlattices. Science 2016, 351, 582–586.
- (23) He, M.; Gales, J. P.; Ducrot, É.; Gong, Z.; Yi, G.-R.; Sacanna, S.; Pine, D. J. Colloidal diamond. *Nature* **2020**, *585*, 524–529.
- (24) Rechtsman, M. C.; Stillinger, F. H.; Torquato, S. Synthetic diamond and wurtzite structures self-assemble with isotropic pair interactions. *Physical Review E* **2007**, *75*, 031403.
- (25) Long, C.; Lei, Q.-L.; Ren, C.-L.; Ma, Y.-Q. Three-dimensional non-close-packed structures of oppositely charged colloids driven by pH oscillation. *The Journal of Physical Chemistry B* **2018**, *122*, 3196–3201.
- (26) Romano, F.; Sciortino, F. Patterning symmetry in the rational design of colloidal crystals. *Nature Communications* **2012**, *3*, 975.
- (27) Chen, D.; Zhang, G.; Torquato, S. Inverse design of colloidal crystals via optimized patchy interactions. *The Journal of Physical Chemistry B* **2018**, *122*, 8462–8468.
- (28) Lindquist, B. A.; Jadrich, R. B.; Truskett, T. M. Communication: Inverse design for self-assembly via on-the-fly optimization. The Journal of Chemical Physics 2016, 145, 111101.
- (29) Escobedo, F. A. Optimizing the formation of colloidal compounds with components of different shapes. *The Journal of Chemical Physics* **2017**, *147*, 214501.
- (30) Rechtsman, M. C.; Stillinger, F. H.; Torquato, S. Optimized interactions for targeted

- self-assembly: application to a honeycomb lattice. *Physical Review Letters* **2005**, *95*, 228301.
- (31) Jain, A.; Errington, J. R.; Truskett, T. M. Dimensionality and design of isotropic interactions that stabilize honeycomb, square, simple cubic, and diamond lattices. *Physical Review X* **2014**, *4*, 031049.
- (32) Torquato, S. Inverse optimization techniques for targeted self-assembly. *Soft Matter* **2009**, *5*, 1157–1173.
- (33) Marcotte, E.; Stillinger, F. H.; Torquato, S. Communication: Designed diamond ground state via optimized isotropic monotonic pair potentials. *The Journal of Chemical Physics* **2013**, *138*, 061101.
- (34) Ferguson, A. L. Machine learning and data science in soft materials engineering. *Journal of Physics: Condensed Matter* **2017**, *30*, 043002.
- (35) Rao, A. B.; Shaw, J.; Neophytou, A.; Morphew, D.; Sciortino, F.; Johnston, R. L.; Chakrabarti, D. Leveraging hierarchical self-assembly pathways for realizing colloidal photonic crystals. *ACS Nano* **2020**, *14*, 5348–5359.
- (36) Ma, Y.; Ferguson, A. L. Inverse design of self-assembling colloidal crystals with omnidirectional photonic bandgaps. *Soft Matter* **2019**, *15*, 8808–8826.
- (37) Wang, L.; Xia, L.; Li, G.; Ravaine, S.; Zhao, X. S. Patterning the surface of colloidal microspheres and fabrication of nonspherical particles. *Angewandte Chemie International Edition* **2008**, *47*, 4725–4728.
- (38) Bae, C.; Moon, J.; Shin, H.; Kim, J.; Sung, M. M. Fabrication of monodisperse asymmetric colloidal clusters by using contact area lithography (CAL). *Journal of the American Chemical Society* **2007**, *129*, 14232–14239.

- (39) Kamp, M.; de Nijs, B.; van der Linden, M. N.; de Feijter, I.; Lefferts, M. J.; Aloi, A.; Griffiths, J.; Baumberg, J. J.; Voets, I. K.; van Blaaderen, A. Multivalent patchy colloids for quantitative 3D self-assembly studies. *Langmuir* **2020**, *36*, 2403–2418.
- (40) Perry, R. W.; Manoharan, V. N. Segregation of "isotope" particles within colloidal molecules. *Soft Matter* **2016**, *12*, 2868–2876.
- (41) McGinley, J. T.; Wang, Y.; Jenkins, I. C.; Sinno, T.; Crocker, J. C. Crystal-templated colloidal clusters exhibit directional dna interactions. *ACS Nano* **2015**, *9*, 10817–10825.
- (42) Jo, I.-S.; Oh, J. S.; Kim, S.-H.; Pine, D. J.; Yi, G.-R. Compressible colloidal clusters from Pickering emulsions and their DNA functionalization. *Chemical Communications* **2018**, *54*, 8328–8331.
- (43) Duguet, E.; Désert, A.; Perro, A.; Ravaine, S. Design and elaboration of colloidal molecules: An overview. *Chemical Society Reviews* **2011**, *40*, 941–960.
- (44) Chen, H.; Zhang, W.; Wang, Z. Comparative studies on photonic band structures of diamond and hexagonal diamond using the multiple scattering method. *Journal of Physics: Condensed Matter* **2004**, *16*, 741–748.
- (45) Chen, Q.; Bae, S. C.; Granick, S. Staged self-assembly of colloidal metastructures.

 Journal of the American Chemical Society 2012, 134, 11080–11083.
- (46) Li, W.; Palis, H.; Mérindol, R.; Majimel, J.; Ravaine, S.; Duguet, E. Colloidal molecules and patchy particles: Complementary concepts, synthesis and self-assembly. *Chemical Society Reviews* 2020, 49, 1955–1976.
- (47) Wang, Y.; Wang, Y.; Zheng, X.; Yi, G.-R.; Sacanna, S.; Pine, D. J.; Weck, M. Three-dimensional lock and key colloids. *Journal of the American Chemical Society* **2014**, 136, 6866–6869.

- (48) Choueiri, R. M.; Galati, E.; Thérien-Aubin, H.; Klinkova, A.; Larin, E. M.; Querejeta-Fernández, A.; Han, L.; Xin, H. L.; Gang, O.; Zhulina, E. B. et al. Surface patterning of nanoparticles with polymer patches. *Nature* **2016**, *538*, 79–83.
- (49) Humphrey, W.; Dalke, A.; Schulten, K. VMD: Visual molecular dynamics. *Journal of Molecular Graphics* **1996**, *14*, 33 38.
- (50) Weeks, J. D.; Chandler, D.; Andersen, H. C. Role of repulsive forces in determining the equilibrium structure of simple liquids. *The Journal of Chemical Physics* **1971**, *54*, 5237–5247.
- (51) Kern, N.; Frenkel, D. Fluid–fluid coexistence in colloidal systems with short-ranged strongly directional attraction. *The Journal of Chemical Physics* **2003**, *118*, 9882–9889.
- (52) Pawar, A. B.; Kretzschmar, I. Patchy particles by glancing angle deposition. *Langmuir* **2008**, *24*, 355–358.
- (53) Pawar, A. B.; Kretzschmar, I. Multifunctional patchy particles by glancing angle deposition. *Langmuir* **2009**, *25*, 9057–9063.
- (54) Anderson, J. A.; Lorenz, C. D.; Travesset, A. General purpose molecular dynamics simulations fully implemented on graphics processing units. *Journal of Computational Physics* **2008**, *227*, 5342 5359.
- (55) Glaser, J.; Nguyen, T. D.; Anderson, J. A.; Lui, P.; Spiga, F.; Millan, J. A.; Morse, D. C.; Glotzer, S. C. Strong scaling of general-purpose molecular dynamics simulations on GPUs. Computer Physics Communications 2015, 192, 97 – 107.
- (56) Hansen, N.; Müller, S. D.; Koumoutsakos, P. Reducing the time complexity of the derandomized evolution strategy with covariance matrix adaptation (CMA-ES). *Evolutionary Computation* **2003**, *11*, 1–18.

- (57) Hansen, N.; Ostermeier, A. Completely Derandomized Self-Adaptation in Evolution Strategies. *Evolutionary Computation* **2001**, *9*, 159–195.
- (58) Qin, J.; Khaira, G. S.; Su, Y.; Garner, G. P.; Miskin, M.; Jaeger, H. M.; de Pablo, J. J. Evolutionary pattern design for copolymer directed self-assembly. Soft Matter 2013, 9, 11467–11472.
- (59) Miskin, M. Z.; Jaeger, H. M. Adapting granular materials through artificial evolution.

 Nature Materials 2013, 12, 326–331.
- (60) Whitesides, G. M.; Grzybowski, B. Self-assembly at all scales. *Science* **2002**, *295*, 2418–2421.
- (61) Steinhardt, P. J.; Nelson, D. R.; Ronchetti, M. Bond-orientational order in liquids and glasses. *Physical Review B* **1983**, *28*, 784–805.
- (62) Lechner, W.; Dellago, C. Accurate determination of crystal structures based on averaged local bond order parameters. *The Journal of Chemical Physics* **2008**, *129*, 114707.
- (63) Johnson, S. G.; Joannopoulos, J. D. Block-iterative frequency-domain methods for Maxwell's equations in a planewave basis. *Optics Express* **2001**, *8*, 173–190.
- (64) Perro, A.; Duguet, E.; Lambert, O.; Taveau, J.-C.; Bourgeat-Lami, E.; Ravaine, S. A chemical synthetic route towards "colloidal molecules". Angewandte Chemie International Edition 2009, 48, 361–365.
- (65) Manoharan, V. N.; Elsesser, M. T.; Pine, D. J. Dense packing and symmetry in small clusters of microspheres. *Science* **2003**, *301*, 483–487.
- (66) Wang, Y.; Wang, Y.; Breed, D. R.; Manoharan, V. N.; Feng, L.; Hollingsworth, A. D.; Weck, M.; Pine, D. J. Colloids with valence and specific directional bonding. *Nature* 2012, 491, 51–55.

- (67) Wang, Y.; Wang, Y.; Zheng, X.; Ducrot, É.; Yodh, J. S.; Weck, M.; Pine, D. J. Crystallization of DNA-coated colloids. *Nature Communications* **2015**, *6*, 7253.
- (68) Rogers, W. B.; Crocker, J. C. Direct measurements of DNA-mediated colloidal interactions and their quantitative modeling. Proceedings of the National Academy of Sciences of the United States of America 2011, 108, 15687–15692.
- (69) Henzie, J.; Grünwald, M.; Widmer-Cooper, A.; Geissler, P. L.; Yang, P. Self-assembly of uniform polyhedral silver nanocrystals into densest packings and exotic superlattices.

 Nature Materials 2012, 11, 131–137.
- (70) Oliveira, R.; Ott, L.; Ramos, F. Bayesian optimisation under uncertain inputs. arXiv preprint arXiv:1902.07908 2019,
- (71) Yan, J.; Bloom, M.; Bae, S. C.; Luijten, E.; Granick, S. Linking synchronization to self-assembly using magnetic Janus colloids. *Nature* **2012**, *491*, 578–581.

TOC Graphic

